AIP | Conference Proceedings

# Super-elastic response of metals to laser-induced shock waves

V. V. Zhakhovsky, B. J. Demaske, N. A. Inogamov, V. A. Khokhlov, S. I. Ashitkov et al.

Citation: AIP Conf. Proc. **1464**, 102 (2012); doi: 10.1063/1.4739864
View online: http://dx.doi.org/10.1063/1.4739864
View Table of Contents: http://proceedings.aip.org/dbt/dbt.jsp?KEY=APCPCS&Volume=1464&Issue=1
Published by the American Institute of Physics.

---

## Related Articles

Lattice strain of osmium diboride under high pressure and nonhydrostatic stress
J. Appl. Phys. 112, 013526 (2012)

Elastic constants of langasite and alpha quartz at high temperatures measured by antenna transmission acoustic resonance
Rev. Sci. Instrum. 83, 073901 (2012)

Transferable pair potentials for CdS and ZnS crystals
J. Chem. Phys. 136, 234111 (2012)

Statistical description of hydrodynamic processes in ionic melts while taking into account polarization effects
J. Chem. Phys. 136, 234502 (2012)

The structural, dielectric, elastic, and piezoelectric properties of KNbO3 from first-principles methods
J. Appl. Phys. 111, 104107 (2012)

---

## Additional information on AIP Conf. Proc.

Journal Homepage: http://proceedings.aip.org/
Journal Information: http://proceedings.aip.org/about/about_the_proceedings
Top downloads: http://proceedings.aip.org/dbt/most_downloaded.jsp?KEY=APCPCS
Information for Authors: http://proceedings.aip.org/authors/information_for_authors

ADVERTISEMENT

AIP Advances

Explore AIP's new open-access journal

- Article-level metrics now available
- Join the conversation! Rate & comment on articles

Submit Now

Downloaded 08 Aug 2012 to 130.183.86.18. Redistribution subject to AIP license or copyright; see http://proceedings.aip.org/about/rights_permissions

# Super-elastic response of metals to laser-induced shock waves

V. V. Zhakhovsky*, B. J. Demaske*, N. A. Inogamov†, V. A. Khokhlov†,
S. I. Ashitkov**, M. B. Agranat** and I. I. Oleynik*

*Department of Physics, University of South Florida, Tampa, FL 33620, USA
†Landau Institute for Theoretical Physics, RAS, Chernogolovka 142432, Russia
**Joint Institute for High Temperatures, RAS, Moscow 125412, Russia

**Abstract.** The structure and evolution of ultrashort shock waves generated by femtosecond laser pulses were explored in single-crystal nickel films via molecular dynamics and two-temperature hydrodynamics simulations. Ultrafast laser heating induces pressure build-up in a 100-nm-thick layer below the surface of the film. For low-intensity laser pulses, the stress-confined subsurface layer breaks into a single elastic shock wave with an amplitude that may exceed the conventional Hugoniot elastic limit. Comparative analysis with available experimental data confirms the existence of *super*-elastic states attainable through ultrashort shock compression. At high laser intensities, the two shock waves, elastic and plastic, form independently from the initial pressure profile. Because the laser heating was isochoric, the pressure and temperature at the melting front was fixed independent of absorbed fluence and results in a fluence-independent amplitude of the elastic wave generated at the liquid-solid interface. Elastic amplitude does not attenuate during propagation due to support from acoustic pulses emitted by the plastic front; whereas the unsupported plastic front undergoes significant attenuation and may fully decay within the metal film.

## INTRODUCTION

The splitting of shock waves into an elastic precursor and a plastic front is a general phenomena that has been observed in a wide variety of crystalline materials both in experiment [1–4] and, more recently, in molecular dynamics (MD) simulations [5–8]. After many flyer-plate shock compression experiments on millimeter-sized targets, researchers found that the amplitude of the elastic precursor in a given type of material was independent of the impact velocity. In light of this result, the term Hugoniot elastic limit (HEL), taken to be the amplitude of the elastic precursor, was introduced as a measure of the threshold for irreversible plastic deformation under shock compression. The focus on understanding the atomic-scale nature of shock-induced plasticity led to the use of MD simulations to investigate shock waves in solids. Elastic precursor amplitudes in MD simulations, however, where sample thickness is limited to a few microns, were found to consistently overestimate the experimental HEL. Specifically in metals, this difference amounts to roughly two orders of magnitude [1, 9–11]

However, through systematic studies on Al and LiF samples of varying thickness, researchers determined that the HEL is not constant, but decreases nonlinearly with increasing sample thickness [12–14]. Because plasticity consists of many different rate dependent processes, split shock waves propagating over short distances may only acti-

*International Symposium on High Power Laser Ablation 2012*
AIP Conf. Proc. 1464, 102-112 (2012); doi: 10.1063/1.4739864

vate fast processes of plastic deformation, such as homogeneous dislocation nucleation, which have large activation stresses on the order of the shear modulus. In such cases, the amplitude of the elastic precursor, i.e., the HEL, is also large. As propagation distance increases, so to does the separation between the fronts and slow rate processes are then activated, thereby reducing the amplitude of the elastic precursor to its conventional low-stress value. Although instrumental to the development of a rate-dependent model of plasticity, such experiments were not able to resolve shock wave structure on the scales of MD simulations.

In addition to vastly improving the time-resolution of shock compression experiments, ultrashort laser pulses $(0.1\text{-}100 \text{ ps})$ may serve the dual role of shock generator. Ultrafast energy deposition by the laser pulse leads to isochoric heating and pressurization of a narrow subsurface layer of material that later acts as piston driving a shock wave into the target. Recently, shock compression experiments utilizing femtosecond laser pulses were performed on submicron-sized Ni films [15]. For such short duration pulses, the piston acts over a very short time, thus producing a shock wave that moves through the target unsupported. Interestingly, these experiments found a faster-than-expected plastic shock wave incident at the rear surface. Through comparative analysis of experimental and simulated data, we show that the anomalously high speed of the shock wave can be explained only if the assumption of a plastic wave is discarded. In reality, the observed shock waves were elastic despite amplitudes several times greater than the conventional HEL determined for millimeter-sized samples. This conclusion is further strengthened by recent experiments [16–20], where elastic amplitudes in micron-sized Al films were found to be in good agreement with those obtained in MD simulations [11, 21]. Because the HEL is a function of propagation distance (compression time), such an observation is not entirely surprising. However, as we will show in the second part of this work, ultrashort shock waves can remain elastic for pressures almost two times greater than the simulated HEL. It is only at much higher pressures, generated by high-intensity laser pulses, that a secondary plastic front develops.

## COMPUTATIONAL MODEL

In metals, the energy of the incident laser pulse is absorbed by conduction electrons within a skin layer of $\sim 10$ nm. After ultrafast internal thermalization of the electronic subsystem, the hot conduction electrons diffuse into the metal and exchange energy with the surrounding ions [22]. Within a time $\tau$ following laser absorption, where $\tau \approx 7$ ps for Ni, the electronic and ionic subsystems reach thermal equilibrium. At which point the laser heating has penetrated a depth $d_T$. For most metals including Ni, $\tau$ is less than the acoustic time $t_s = d_T/c_s$, where $c_s$ is the longitudinal sound speed of the irradiated material. If the thickness of the film $l_x > t_s c_s$, then there is minimal thermal expansion at times prior to $\tau$ and a highly-pressurized, *stress-confined*, layer forms below the irradiated surface [23].

The laser-metal interaction is divided into two coupled stages. The first stage, including laser energy absorption and electron-ion thermalization, was simulated by a one-dimensional hydrodynamics code based on the well-known two-temperature model [24].

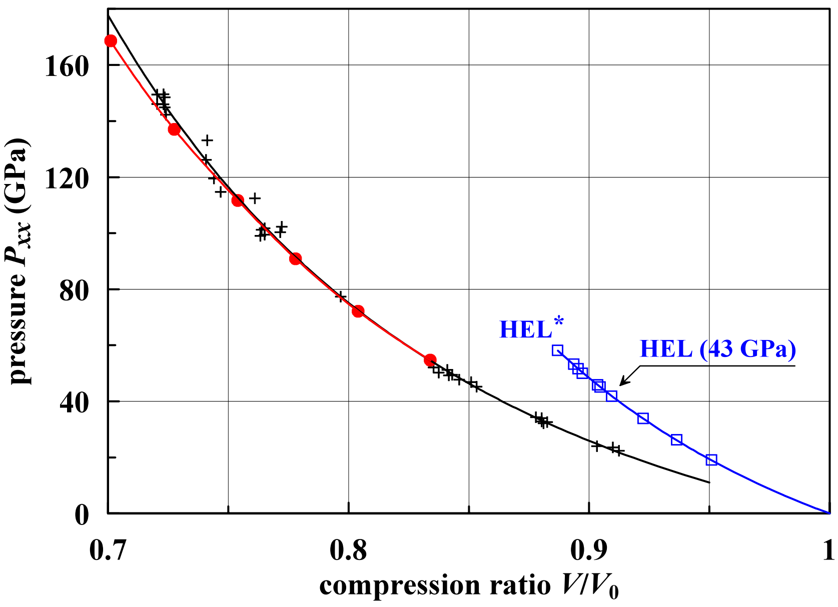

**FIGURE 1.** $P-V$ Hugoniot for shock compression of single-crystalline Nickel in the $\langle 110 \rangle$ direction. Circles give simulated points along the plastic branch and squares along the elastic branch. Crosses are taken from an experimental database [25]. The simulated Hugoniot elastic limit (HEL) is shown for micron-sized samples with a random distribution of vacancies at a concentration of 0.1%. The *metastable* elastic states are allocated between the HEL and the ultrashort-lived state $\mathrm{HEL}^*$ having $P \approx 58$ GPa.

The second stage, which includes all physical processes originating from interactions among ions, was simulated by nonequilibrium MD. The 2T-HD and MD simulations were linked via the one-dimensional temperature distribution of the film at the end of the two-temperature stage, $t = \tau$, which has an approximately Gaussian form.

$$T(x) = T_1 e^{-x^2/d_T^2} + 300\ \mathrm{K} \tag{1}$$

Using $T(x)$ as input for a Langevin thermostat that ran during the electron-ion thermalization time $\tau$, the laser heating was effectively reproduced in MD simulations. The absorbed fluence was controlled by adjusting the maximum surface temperature $T_s = T(0) = T_1 + 300$ K. For high-intensity laser irradiation, the electron subsystem is strongly excited and associated phenomena, e.g. plasma formation, lie outside the domain of classical MD methods. However, in the scope of this work, such surface phenomena can be ignored as they have no effect on the processes in the bulk and rear of the film.

In order to accurately describe materials response at the high temperature and pressure conditions induced by femtosecond laser heating, we have employed a new embedded atom method (EAM) interatomic potential for Ni in our MD simulations. Following the approach of Ref. [26], the potential was fit to cold pressure curves calculated by density-functional theory for a wide range of hydrostatic and uniaxial deformations as well as to experimental properties near equilibrium, such as lattice constant, cohesive energy, elastic constants, and stacking fault and vacancy formation energies. The melting point at zero pressure of the new EAM potential $T_m = 1711$ K is in good agreement with the

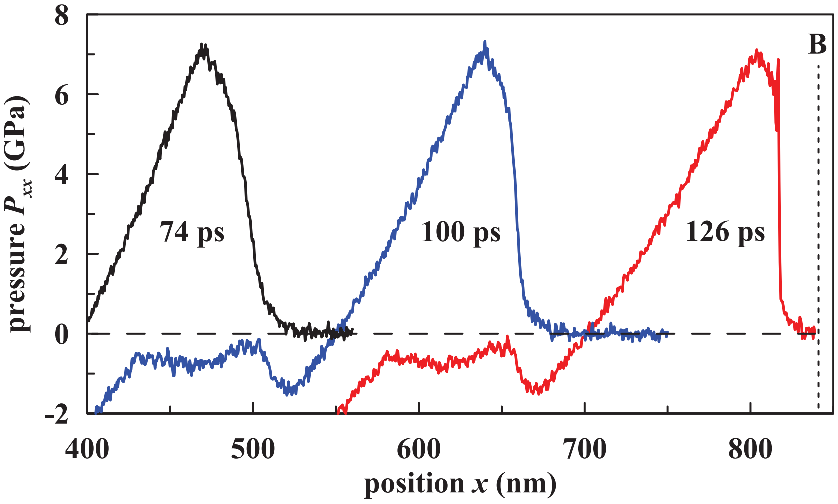

**FIGURE 2.** Several snapshots from a molecular dynamics simulation of an ultrashort elastic wave propagating in an 839 nm Nickel film. Process of wave-breaking proceeds slowly and a fully-developed shock is not visible until reaching the edge of the sample, shown by the vertical dotted line B.

experimental value of 1728 K [27]. The principal Hugoniot for the new EAM potential is shown in Fig. 1 plotted against experimental data [25]. Good agreement along the plastic branch ensures the interatomic potential provides a reliable description of Ni under shock compression.

Our MD samples had dimensions $l_x \times l_y \times l_z$ with $l_x$ oriented along the direction of the incident laser pulse and periodic boundary conditions imposed along the transverse dimensions $l_y$ and $l_z$. Sample thicknesses were chosen to reproduce those used in Ref. [15]. The glass substrate used in experiment was approximated by a 250-nm-thick layer of Ni crystal with the same orientation as the film, but with a density $\rho$ modified to reproduce the acoustic impedance $Z = c_s\sqrt{\rho\rho_{Ni}}$ of glass, where $c_s$ is the longitudinal sound speed of the original Ni crystal. For single-crystal samples oriented in the $\langle 110 \rangle$ direction, $\rho = 0.047\rho_{Ni}$. All presented simulations are for samples with a cross-section of $16 \times 12\,\mathrm{nm}^2$. Almost no dependence of the simulated results for cross-sections $> 8 \times 8\ \mathrm{nm}^2$ was observed.

## SIMULATION RESULTS

The simulation results are divided into three sections. In the first section, simulations are presented for weak elastic shock waves in Ni films deposited on glass irradiated by low-intensity femtosecond laser pulses and are directly related to experiments described in Ref. [15]. The second section extends the simulations to higher laser intensities, where a transition from single elastic to split elastic and plastic shock waves was found. Simulations within the split wave regime are presented in the final section. For femtosecond laser pulse intensities $> 10^{13}$ W/cm$^2$, optical breakdown of the glass occurs, thereby preventing any laser energy transmission to the metal surface [31]. In

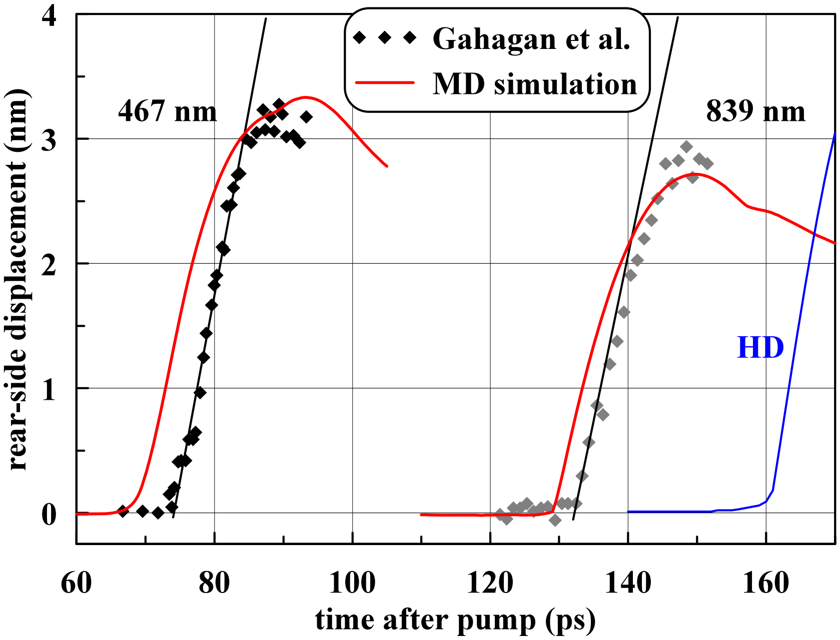

**FIGURE 3.** Rear-side displacement as a function of time after laser pulse firing for 839 and 467 nm film. Results from molecular dynamics (MD) and hydrodynamics (HD) simulation are shown by solid lines. Diamonds are experimental points transformed from raw data in Ref. [15]. Final free surface velocities $u_f$ were obtained by linear fits to the experimental data.

order to maintain a close link to experimental conditions, the glass layer was removed for simulations presented in the final two sections.

## Weak elastic shock waves

Laser heating induces melting of a 100-nm-thick layer at the irradiated surface. Upon expansion of the molten Ni at the glass boundary, a compression wave formed that began to propagate towards the rear surface of the film. Due to an increase in the local sound speed with compression, the velocity of the leading part of the wave was less than the that of the peak. In time, the wave front steepened (focusing of characteristics) as illustrated in Fig. 2. The process of wave-breaking proceeded slowly, and a well-developed shock wave, i.e., one with a rise time equal to only a few lattice spacings, was observed only for the thickest (839 nm) film. For the thinner films, the incident wave at the rear surface was not a shock, but a sharp compression wave. The absorbed fluence $F_{abs}$ was varied until a shock wave with an amplitude of $\approx 8$ GPa was generated, the same as in experiment [15]. With introduction of a grain boundary along the shock wave propagation direction, materials response remained elastic.

For weak shock waves, the shock velocity $u_s$ differs only marginally from the longitudinal sound speed $c_s$. For simulated Ni single-crystal samples at zero temperature, $c_s$ is equal to 5.38, 6.12, and 6.35 km/s, for orientations $\langle 100 \rangle$, $\langle 110 \rangle$, and $\langle 111 \rangle$, respectively. For polycrystalline films, typical of the vapor-deposited Ni films used in

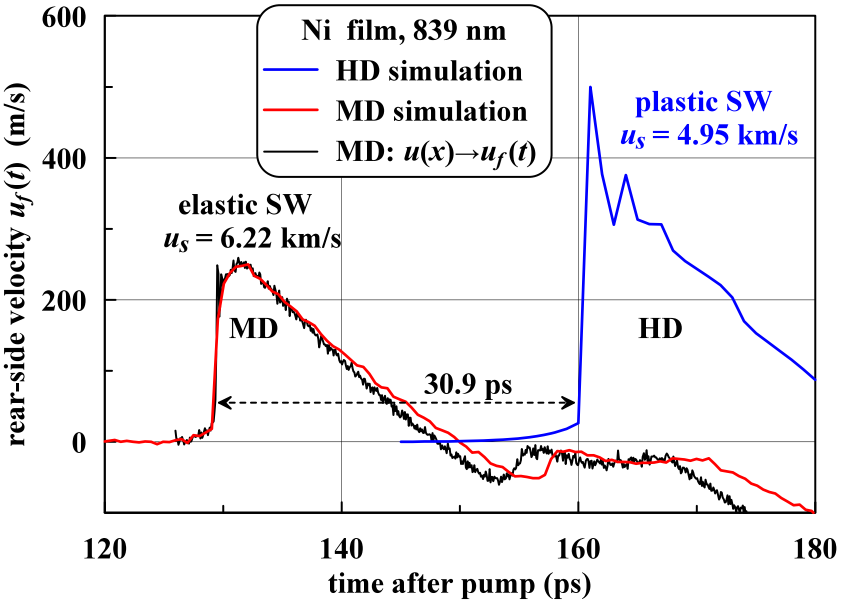

**FIGURE 4.** Rear-side velocity histories upon shock wave arrival from molecular dynamics (MD) and hydrodynamics (HD) simulations of an 839 nm film irradiated by a low-intensity femtosecond laser pulse. A strong plastic shock wave simulated by HD arrives at rear surface much later than the elastic shock wave simulated by MD.

experiment, the local value for $c_s$ within a given grain will depend on the orientation. If these orientations are assumed to be uniformly and randomly distributed throughout the material, then the corresponding value of $c_s$ for the material as a whole should approach the average taken over all possible crystallographic directions. It follows that the $\langle 110 \rangle$ direction should best reproduce the sound speed of samples used in experiment as it is closest to the average of the three major cubic crystal directions. Indeed, it was found that the shock wave propagating in the $\langle 110 \rangle$ direction arrived only a few picoseconds before the one from experiment, see Fig. 3, while those propagating in the $\langle 100 \rangle$ and $\langle 111 \rangle$ directions arrived slightly later and earlier, respectively. The plastic shock wave simulated by HD arrived much later $(30.95\text{ ps})$ than the elastic shock wave simulated by MD, which had an arrival time only a few picoseconds less than experiment. The average velocity of the plastic shock wave was $5\text{ km/s}$, much less than the average shock velocities in both experiment and MD simulations. Therefore, we think the shock waves observed in Ni films by Ref. [15] were pure elastic waves.

The responses of the rear free surfaces of 467 and 839 nm films are shown in Figs. 3 and 4. The final free surface velocity after arrival of the shock wave $u_f$ was obtained by a linear fit to the experimental rear surface displacement profile at shock wave breakout. For a free surface in vacuum, the final particle velocity is $u_p = u_f/2$ as follows from the acoustic approximation. The corresponding values for $u_p$ for an 839 nm film obtained from experiment and MD simulations are 265 and 260 m/s, respectively. Assuming the structure of the shock wave is known, $u_s$ can be determined from the appropriate $u_p - u_s$ Hugoniot. The corresponding relation used in experiment, where plastic shock waves were *assumed*, is $u_s = 4.60 + 1.437 u_p$, whereas the relation for the elastic shock waves simulated by MD is $u_s = 5.98 + 1.881u_p$. Using the respective equations, the *calculated* values for $u_s$ for 839 nm films in experiment and MD simulation are 4.98 and 6.22 km/s, respectively. The experimental $u_s = 4.98$ km/s estimated from plastic Hugoniot is well below the directly measured value of shock-wave speed $u_s = 6.15$ km/s discussed in the next section.

In experiment, the shock wave breakout time relative to pump pulse firing time was known. Using a measurement of the propagation time for a thin $\sim 50$ nm film, the propagation times were then determined and used to calculate the average shock velocity $\overline{u_s}$ [15]. For 839 nm film, $\overline{u_s}$ had a *measured* value of $6.15 \pm 0.39$ km/s, which is comparable to the value of 6.28 km/s obtained directly from our MD simulation. Similar agreement between the simulated and experimental values for $\overline{u_s}$ was also obtained for the cases of 467 and 250 nm films. Due to the rarefaction tail, the shock wave was attenuated as it propagated through the sample. As an illustration of this effect on $u_s$ for the case of an 839 nm film, consider the initial value of 6.35 km/s obtained directly from simulation. Comparing this value to $u_s$ at breakout, the rate of attenuation of $u_s$ was small.

To confirms the good accuracy of relation $u_p = u_f/2$ used to obtain the particle velocity in experiments, the rear surface velocities from HD and MD simulations of an 839 nm film shown in Fig. 4 were used to check the acoustic approximation. The simple velocity transformation $u_f(t) = 2u_p(x/c_s)$ was applied to the simulated spatial profile of the particle velocity $u_p(x)$ within the shock wave arriving at the rear surface at $x = 0$, which are given by the left dashed and solid lines in Fig. 4. Because the transformed data is in good agreement with the velocity profile obtained directly from MD simulation, the relation $u_p = u_f/2$ gives an accurate estimate of particle velocity in a simulated elastic shock wave with amplitude of $\sim 8$ GPa.

## Strong elastic shock waves

We performed a series of simulations in 839 nm films for different values of $F_{abs}$. It was found that the laser heating was isochoric within the first few picoseconds $(t_{iso} < \tau)$ of simulation. Material heated to states far above the melting curve was melted supersonically relative to the solid material ahead of it, see Fig. 6. Moreover, because the heating was isochoric, the pressure and temperature at the melting front was fixed independent of absorbed fluence. To compensate, higher absorbed fluences had larger molten zones.

For times $t_{iso} < t < \tau$, shear stresses became nonzero at the edge of the liquid-solid interface signaling the end of isochoric heating and the beginning of uniaxial compression associated with wave dynamics. During this stage of laser heating, the pressure at the melting front rose due to propagation of the compression wave into the solid. Concurrently, the temperature at the melting front rose due to a combination of isochoric heating by the thermostat and adiabatic heating by the compression wave. This heating led to melting of new material, albeit at a now subsonic rate due to the constantly rising pressure, see Fig. 6. Because the state of the material at the melting front was determined by the melting curve, this limited the amplitude of the transmitted

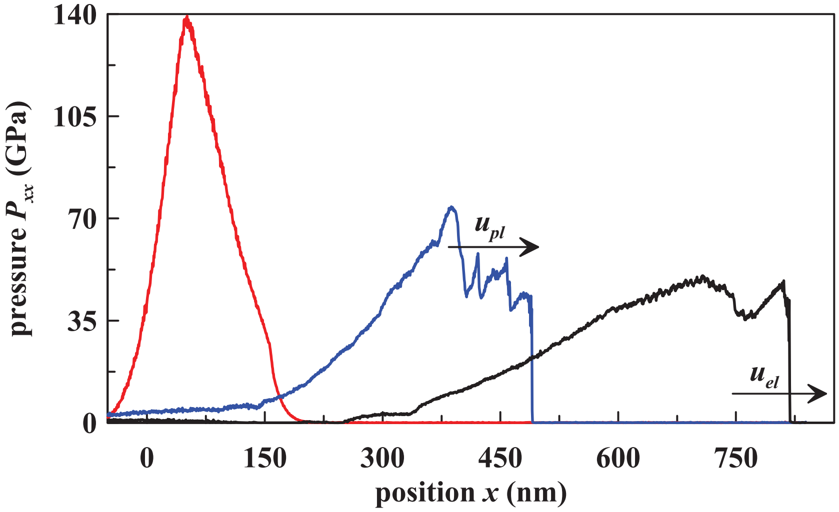

**FIGURE 5.** From left to right, snapshots at times 10, 48, and 93 ps from a molecular dynamics simulation of an 839 nm Nickel film irradiated by a high-intensity femtosecond laser pulse. The strong compression wave at 10 ps breaks into a fast elastic shock wave with velocity $u_{el}$ followed closely by a rapidly attenuating plastic front of velocity $u_{pl}$. By 93 ps, the plastic front has decayed completely.

compression wave.

For absorbed fluences $< 0.6\ \mathrm{J/cm^2}$, the compression wave formed after laser heating broke into a single elastic shock wave with an amplitude dependent on laser fluence. The time required for wave-breaking was also considerably less than for weak shocks and decreased with increasing absorbed fluence. For a simulation at the fluence threshold, the pressure at the central part of the liquid metal layer immediately after laser heating was in excess of 80 GPa, whereas the pressure at the liquid-solid interface was significantly lower, $\approx 50$ GPa. Although some plastic deformation developed at the edge of the melting front, no plastic wave was formed and the compression wave broke into a single elastic shock wave with an amplitude almost two times greater than the HEL determined from MD simulations of Ni samples, where $P_{HEL} = 43$ GPa shown in Fig. 1. A typical material particle traveling through the elastic shock front was uniaxially compressed to pressures $> P_{HEL}$ for $\approx 20$ ps.

## Split elastic and plastic shock waves

For simulations with absorbed fluences $> 0.6\ \mathrm{J/cm^2}$, we observed the process of double wave-breaking in which an elastic wave formed followed closely by a plastic wave, see Fig. 5. Independent of absorbed fluence, the amplitude of the elastic precursor was $\sim 45$ GPa. Generation of dislocations near the plastic front resulted in a sudden release of shear stress and emission of an acoustic pulse into the elastic zone. These pulses traveled within the elastically compressed material at a velocity greater than the leading elastic front. In a manner similar to steady two-zone elastic-plastic shock waves [11], the acoustic pulses supported the motion of the elastic front. Presence of these

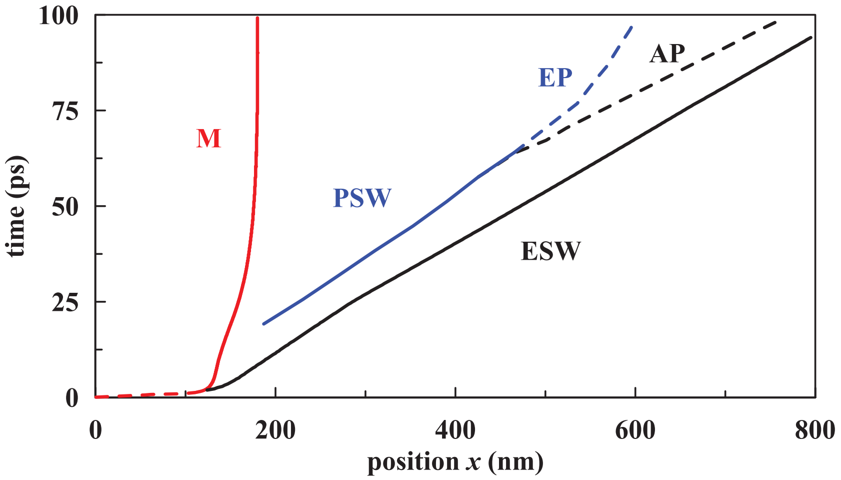

**FIGURE 6.** Trajectories of the melting front (M), elastic shock wave (ESW), and plastic front (PF) in a molecular dynamics simulation of a 839 nm Nickel film irradiated by a high-intensity femtosecond laser pulse. Dashed line preceding the melting front indicates bulk melting during the initial laser heating. At $\sim 60$ ps, the PF is extinguished after emitting a final acoustic pulse (AP). The elastic-plastic transition layer (EP) continues to propagate, but rapidly decelerates reaching a final depth of $\sim 600$ nm.

pulses caused the pressure within the elastic zone to fluctuate and at times the pressure would jump to 55 GPa, which is close to the upper limit of the metastable elastic branch of the Hugoniot HEL$^*$ shown in Fig. 1.

The trajectories of the elastic and plastic fronts are shown in Fig. 6 for a simulation at an absorbed fluence of $1.57\ \mathrm{J/cm^2}$. Initially, the plastic front had a velocity almost equal to that of the elastic front. As the simulation progressed, the plastic front was attenuated by the rarefaction tail. Once its amplitude dropped below 55 GPa the plastic wave emitted a final acoustic pulse and decayed into a subsonic front, shown by the dashed lines labeled AP and EP in Fig. 6. The subsonic front is not a wave, but instead represents the separating layer between the plastic and elastic material states. The transition layer propagates within the elastically compressed material as a result of the multiplication of preexisting dislocations at the edge of the plastic zone. Due to the relatively small thicknesses of the simulated films, the exact motion of the elastic-plastic transition layer was complicated by the reflection of the shock wave at the rear side. Although, for thicker films, it can be assumed that the transition layer attains some final constant depth.

## DISCUSSION

We propose that the shock waves observed in Ref. [15] were elastic despite amplitudes several times greater than the conventional HEL determined from shock compression experiments performed on millimeter-sized samples [1, 3]. To summarize, the maximum free surface velocities $u_f$ obtained from MD simulations of elastic shock waves were in good agreement with those measured in experiment. Second, the average shock velocities $\overline{u_s}$ measured in experiment were considerably more than the shock velocity at breakout $u_s$ obtained from fitting $u_p = u_f/2$ to the plastic branch of the $u_p - u_s$ Hugoniot. Moreover, we showed using the results of our simulations that attenuation of the shock wave during propagation was minor and could not account for the large discrepancy between the two experimental measurements of $u_s$. Lastly, we showed that a strong plastic shock wave simulated by HD arrived at the rear surface much later than shock waves from both MD simulation and experiment. Therefore, a plastic shock wave of comparable amplitude to that observed in experiment would have been considerably slower.

The anomalous elastic behavior of ultrashort shock waves is a result of the *finite* characteristic time of elastic-plastic transformations $\tau_p$. We can expect that as long as the shock wave loading time $t_c \leq \tau_p$, then plastic deformation associated with generation and motion of dislocations will have insufficient time to develop after the shock wave and a plastic front will not form. Indeed, our MD simulations show that a purely elastic response is possible for shock waves with amplitudes $> P_{HEL}$. However, simulations also show that once $F_{abs}$ exceeds some critical value $\approx 0.6$ J/cm$^2$, the compression wave produced during laser heating will transform into a plastic wave and an elastic precursor. Because the heating depth $d_T$ and, consequently, the loading time $t_c$ associated with the initial compression wave changes little with absorbed fluence, then $\tau_p$ must decrease monotonically with increasing pressure. The opposite must also be true as was evident in MD simulation when attenuation caused the plastic front to decay into an acoustic pulse during propagation to the rear side of the film. For a given material with a fixed initial state such that $\tau_p$ is a function of pressure only, the minimum amplitude of the compression wave necessary for formation of a plastic wave should depend solely on the loading time $t_c$.

## CONCLUSIONS

We showed that ultrashort shock waves generated by femtosecond laser pulses behave very differently than their steady counterparts. Two examples of this unusual behavior highlighted in this work are the existence of single elastic ultrashort shock waves with amplitudes greater than $P_{HEL}$ (both the conventional value and from MD simulation) and, within the split wave regime, the attenuation and possible extinction of the plastic front within the metal film. Based on our simulation results, we claim the shock waves observed in Ni films by Ref. [15] were elastic. This claim is supported by the recent experimental observations of high-pressure elastic ultrashort shock waves in Al [16–18, 20]. Making use of the latter property of ultrashort shock waves, we believe it is possible, at least in principle, to localize plastic deformation near the surface of a sample by controlling the intensity of the incident laser pulse.

## ACKNOWLEDGMENTS

This work was supported by the ONR, NRL and NSF. Calculations were performed using NSF TeraGrid facilities, the USF Research Computing Cluster, and computational

facilities of the Materials Simulation Laboratory at USF Physics Department.

## REFERENCES

1. Kanel, G. I., Razorenov, S. V., and Fortov, V. E., *Shock-Wave Phenomena and the Properties of Condensed Matter*, Springer, 2004.
2. Zel'dovich, Y. B., and Raizer, Y. P., *Physics of Shock Waves and High-Temperature Hydrodynamic Phenomena*, Dover, 2002.
3. Graham, R. A., *Solids under high-pressure shock compression: mechanics, physics, and chemistry*, Springer, 1993.
4. Caldirola, P., and Knoepfel, H., editors, *Shock waves in condensed media*, Academic Press, 1971.
5. Germann, T. C., Holian, B. L., Lomdahl, P. S., and Ravelo, R., *Phys. Rev. Lett.*, **84**, 5351–5354 (2000).
6. Zhakhovskii, V. V., Zybin, S. V., Nishihara, K., and Anisimov, S. I., *Phys. Rev. Lett.*, **83**, 1175–1178 (1999).
7. Holian, B. L., *Phys. Rev. A*, **37**, 2562–2568 (1988).
8. Zybin, S. V., Elert, M. L., and White, C. T., *Phys. Rev. B*, **66**, 220102 (2002).
9. Bringa, E. M., Cazamias, J. U., Erhart, P., Stölken, J., Tanushev, N., Wirth, B. D., Rudd, R. E., and Caturla, M. J., *J. Appl. Phys.*, **96**, 3793–3799 (2004).
10. Jarmakani, H., Bringa, E., Erhart, P., Remington, B., Wang, Y., Vo, N., and Meyers, M., *Acta Materialia*, **56**, 5584 – 5604 (2008).
11. Zhakhovsky, V. V., Budzevich, M. M., Inogamov, N. A., Oleynik, I. I., and White, C. T., *Phys. Rev. Lett.*, **107**, 135502 (2011).
12. Arvidsson, T. E., Gupta, Y. M., and Duvall, G. E., *J. Appl. Phys.*, **46**, 4474–4478 (1975).
13. Asay, J. R., Fowles, G. R., Durall, G. E., Miles, M. H., and Tinder, R. F., *Journal of Applied Physics*, **43**, 2132–2145 (1972).
14. Gupta, Y. M., *Journal of Applied Physics*, **46**, 3395–3401 (1975).
15. Gahagan, K. T., Moore, D. S., Funk, D. J., Rabie, R. L., Buelow, S. J., and W., N. J., *Phys. Rev. Lett.*, **85**, 3205–3208 (2000).
16. Ashitkov, S. I., Agranat, M. B., Kanel', G. I., Komarov, P. S., and Fortov, V. E., *JETP Lett.*, **92**, 516–520 (2010).
17. Winey, J. M., LaLone, B. M., Trivedi, P. B., and Gupta, Y. M., *J. Appl. Phys.*, **106**, 073508 (2009).
18. Whitley, V. H., McGrane, S. D., Eakins, D. E., Bolme, C. A., Moore, D. S., and Bingert, J. F., *J. Appl. Phys.*, **109**, 013505 (2011).
19. Crowhurst, J. C., Armstrong, M. R., Knight, K. B., Zaug, J. M., and Behymer, E. M., *Phys. Rev. Lett.*, **107**, 144302 (2011).
20. Huang, Y. Y. W. Y. Z. Z., L., and Su, W., *J. Phys. D.*, **42**, 045502 (2009).
21. Zhakhovskii, V. V., and Inogamov, N. A., *JETP Lett.*, **92**, 521–526 (2010).
22. Anisimov, S. I., and Luk'yanchuk, B., *Phy. Usp.*, **45**, 293 (2002).
23. Demaske, B., Zhakhovsky, V. V., Inogamov, N. A., and Oleynik, I. I., *Phys. Rev. B*, **82**, 064113 (2010).
24. Anisimov, K. B., S.I., and Perel'man, T., *Zh. Eksp. Teor. Fiz.*, **66**, 776 (1974).
25. Shock wave database: http://teos.ficp.ac.ru/rusbank/.
26. Zhakhovskii, V. V., Inogamov, N. A., Petrov, Y. V., Ashitkov, S. I., and Nishihara, K., *Appl. Surf. Sci.*, **255**, 9592–9596 (2009).
27. Lide, D., *CRC handbook of chemistry and physics: a ready-reference book of chemical and physical data*, CRC Handbook of Chemistry and Physics, 85th Ed, CRC Press, (2004).
28. Japel, S., Schwager, N., Boehler, R., and Ross, M., *Phys. Rev. Lett.*, **95**, 167801 (2005).
29. Errandonea, D., Schwager, B., Ditz, R., Boehler, R., and Ross, M., *Phys. Rev. B.*, **63**, 132104 (2001).
30. Lazor, P., Shen, G., and Saxena, S. K., *Phys. Chem. Miner.*, **20**, 86 (1993).
31. von der Linde, D., and Schüler, H., *J. Opt. Soc. Am. B*, **13**, 216–222 (1996).